PROCEEDINGS, Thirty-Eighth Workshop on Geothermal Reservoir Engineering
Stanford University, Stanford, California, February 11-13, 2013
SGP-TR-198

DIRECTLY IMAGING STEEP FAULT ZONES USING MULTICOMPONENT SEISMIC DATA

Ting Chen and Lianjie Huang

Los Alamos National Laboratory
Geophysics Group, MS D452
Los Alamos, NM 87545, USA
E-mails: tchen@lanl.gov (TC); ljh@lanl.gov (LH)

ABSTRACT

Elastic reverse-time migration (ERTM) is the most powerful tool for imaging complex subsurface structures. However, conventional imaging conditions used in ERTM often produce significant artifacts caused by the cross correlation of full wavefields and the polarization of shear waves (S-waves). We use a novel 2D ERTM imaging technique to reduce these artifacts and directly image fault zones. We employ a wavefield separation scheme to obtain downgoing and upgoing waves, and leftgoing and rightgoing waves for both compressional (P) and shear waves within an imaging region. Imaging with these wavefields eliminates the low-wavenumber image noise caused by cross-correlation of full wavefields. We then adopt an imaging condition in the angle domain to properly account for the S-wave polarization, and obtain compressional-to-compressional (PP), compressional -to-shear (PS), shear-to-compressional (SP), and shear-to-shear (SS) images. Our efforts are primarily focused on imaging steeply-dipping fault zones. We validate our ERTM imaging technique using synthetic elastic-wave reflection data for a geophysical model built using geologic features found at the Soda Lake geothermal field, and obtain significantly improved images of the fault zones compared to those obtained using conventional ERTM.

INTRODUCTION

Fault zones may control the flow paths of hot water, or confine the boundaries of geothermal reservoirs. Therefore, imaging fault zones is crucial for geothermal exploration and enhanced geothermal systems.

Prestack depth migration of seismic reflection data is the most robust tool for high-resolution imaging of subsurface structures. Conventional seismic migration uses primary reflections from subsurface interfaces to obtain images of impedance contrasts within subsurface geologic structures. Seismic reflection data often contain no primary reflection waves from steeply-dipping fault zones, and multiple reflections from these fault zones are much weaker than primary reflections from stratigraphic layers. Therefore, it is a great challenge to directly image steeply-dipping fault zones.

Reverse-time migration solves full-wave equation in heterogeneous media, and has the potential to reveal fault zones that are unknown before using single-component seismic data (Huang and Albrecht, 2011; Huang et al., 2011). Elastic reverse-time migration (ERTM) is based on solving the elastic-wave equation in heterogeneous media for forward propagation of wavefields from sources and backward propagation of recorded seismic reflection data from receivers (Baysal et al., 1983; McMechan, 1983; Whitmore, 1983; Chang and McMechan, 1987). ERTM can handle all the complex waveforms and has no dip limitation. It has been shown as the most promising tool for high-resolution images of complex subsurface structures. However, conventional ERTM imaging conditions face some difficulties (Yoon et al., 2004). One of them is the low-wavenumber artifacts in migration images. This is caused by the cross correlation of full waves of source and receiver wavefields, which not only produces images at the reflectors, but also at other locations along the entire wave path. The other difficulty is related to multicomponent seismic data. During elastic-wave propagation, compressional (P) waves can be converted to shear (S) waves, and S waves can be converted to P waves at interfaces. For converted waves, the conventional imaging condition is no longer valid, leading to poor images. This is due to the polarization of converted waves. Destructive interference occurs when stacking PS or SP images with mixed signs of the polarization. Different approaches have been developed to solve these problems (e.g., Mulder and Plessix, 2004; Kaelin and Guitton, 2006; Denli and Huang, 2008; Yan and Xie, 2010; Du et al., 2012).

In this work, we address the challenge of directly imaging steeply-dipping fault zones using surface seismic reflection data. We develop an ERTM technique combining a wavefield-separation imaging condition and an angle-domain imaging condition. We implement this imaging technique for the two-dimensional (2D) case, and apply it to image several steeply-dipping fault zones in a geophysical model built using geologic features found at the Soda Lake geothermal field. Our ERTM results show that this new technique is capable of directly imaging steeply-dipping fault zones, and significantly improves images of the fault zones compared to those obtained using conventional ERTM.

METHOD

In ERTM, the conventional imaging condition for a common-shot gather is given by

$$I(\mathbf{x}) = \int_0^t s(\mathbf{x},\tau) r(\mathbf{x}, t-\tau) d\tau, \qquad (1)$$

where $s(\mathbf{x},\tau)$ is the forward propagation wavefield at spatial location $\mathbf{x}$ and time τ from a source, $r(\mathbf{x}, t-\tau)$ is the backward propagation wavefield from receivers, and t represents the maximum record time.

The conventional imaging condition is simple and straightforward, but it usually generates high-amplitude, low-wavenumber image noise that contaminates and sometimes can even completely mask useful images of interfaces.

To solve this problem, we separate the forward and backward propagation wavefields into upgoing, downgoing, leftgoing, and rightgoing wavefields for both P- and S-waves, and use these wavefields to form multiple images rather than one image in the conventional ERTM (Liu et al., 2011). Therefore, we modify the conventional imaging condition (1) to the cross correlations of separated wavefields propagating along the opposite directions to obtain the downward-looking, upward-looking, left-looking, and right-looking images, given by

$$\begin{aligned}
I^d(\mathbf{x}) &= \int_0^t s^{+z}(\mathbf{x},\tau) r^{-z}(\mathbf{x}, t-\tau) d\tau, \\
I^u(\mathbf{x}) &= \int_0^t s^{-z}(\mathbf{x},\tau) r^{+z}(\mathbf{x}, t-\tau) d\tau, \\
I^r(\mathbf{x}) &= \int_0^t s^{+x}(\mathbf{x},\tau) r^{-x}(\mathbf{x}, t-\tau) d\tau, \\
I^l(\mathbf{x}) &= \int_0^t s^{-x}(\mathbf{x},\tau) r^{+x}(\mathbf{x}, t-\tau) d\tau,
\end{aligned} \qquad (2)$$

where "$+$" and "$-$" refer to wavefields propagating along the opposite directions, "$+x$", "$-x$", "$+z$", and "$-z$" denote rightgoing, leftgoing, downgoing, and upgoing wavefields, respectively. The images I^d, I^u, I^r, and I^l obtained using imaging condition (2) are downward-looking, upward-looking, right-looking, and left-looking images, respectively. The cross correlations of wavefields from opposite directions along the *x*- and *z*-directions give images of vertical (large dip angle) and horizontal (small dip angle) reflectors, respectively.

The destructive images for converted waves are related to stacking of images with mixed signs of polarization. Because the sign of converted PS and SP waves depends on the direction of the incident waves relative to a reflector, we correct for the sign by analyzing the waves in the angle domain, and thus obtain coherent images.

For image analysis in the angle domain, we employ an extended imaging condition given by (Yan and Sava, 2008)

$$I(\mathbf{x},\boldsymbol{\lambda}) = \int s(\mathbf{x}-\boldsymbol{\lambda},\tau) r(\mathbf{x}+\boldsymbol{\lambda}, t-\tau) d\tau, \qquad (3)$$

where $\boldsymbol{\lambda}$ is the cross correlation lag in space. The average angle between incidence and reflected waves, θ, is computed using

$$\tan^2\theta = \frac{(1+\gamma)^2 |\mathbf{k}_\lambda|^2 - (1-\gamma)^2 |\mathbf{k}_\mathbf{x}|^2}{(1+\gamma)^2 |\mathbf{k}_\mathbf{x}|^2 - (1-\gamma)^2 |\mathbf{k}_\lambda|^2}, \qquad (4)$$

where γ is the V_P/V_S ratio for the incident P-wave and the reflected S-wave, and is 1 for non-converted waves. The wavenumbers $\mathbf{k}_\lambda$ and $\mathbf{k}_\mathbf{x}$ are defined using the source and receiver wavenumbers $\mathbf{k}_\mathbf{s}$ and $\mathbf{k}_\mathbf{r}$ as $\mathbf{k}_\lambda = \mathbf{k}_\mathbf{r} + \mathbf{k}_\mathbf{s}$ and $\mathbf{k}_\mathbf{x} = \mathbf{k}_\mathbf{r} - \mathbf{k}_\mathbf{s}$, obtained from $I(\mathbf{x},\boldsymbol{\lambda})$ in equation (3). The angle-domain image gather $I(\mathbf{x},\theta)$ is then obtained from $I(\mathbf{x},\boldsymbol{\lambda})$ using equation (3). The angle-domain migration image is given by

$$A(\mathbf{x}) = \int I(\mathbf{x},\theta)\, d\theta. \qquad (5)$$

We use separated wavefieds to obtain the angle-domain images, and denote migration images obtained using separated wavefields together with an angle-domain imaging condition as A_{pp}, A_{ps}, A_{sp}, and A_{ss}, and those obtained directly from separated wavefields as I_{pp}, I_{ps}, I_{sp}, and I_{ss}. Each of these images has downward-looking, upward-looking, right-looking, and left-looking images obtained using separated wavefields propagation along different directions.

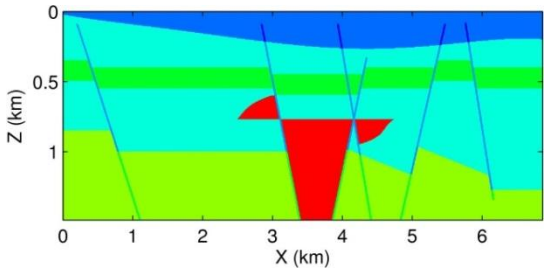

Figure 1: A preliminary velocity model built using geologic features found at the Soda Lake geothermal field, containing several steeply-dipping fault zones.

IMAGING FAULT ZONES

We construct a 2D velocity model using geologic features found in the Soda Lake geothermal field, Nevada, and verify the capability of our 2D elastic-wave reverse-time migration algorithm for imaging steeply-dipping fault zones using synthetic data from the 2D velocity model.

The model is built using the geologic interpretation result of a prestack migration image obtained using seismic data from a 2D East-West line of the seismic survey at the Soda Lake geothermal field. This model consists of five stratigraphic layers and six steeply-dipping fault zones with the width of 25 m (Fig. 1). The model also contains high-contrast basalt units. Velocity and density values of the fault zones are 15% lower than those of the surrounding layers. The ratio of P-wave and S-wave velocities is equal to 2.

We generate synthetic multi-component elastic reflection data for the Soda Lake fault model in Fig. 1 using a high-order finite-difference elastic-wave scheme with a perfectly matched layer absorbing boundary condition. The center frequency of the data is 20 Hz. The source interval is approximately 770 ft, the same as the field seismic survey. For the images shown here, we assume receivers are located at each grid on the surface. Explosive sources are used to study PP and PS images because they have the most incident energy in the P-wave component. Horizontal- and vertical-force sources are used to study SP and SS images because they have significant energy in the incident S-wave component. The wavefield-separation imaging condition is used to obtain all PP, PS, SP, and SS images. The angle-domain imaging condition is further employed to obtained converted PS and SP images.

Figure 2a is the conventional PP image of the Soda Lake fault model using explosive sources. The reflectors are largely masked by the high-amplitude, low-wavenumber background noise caused by the cross correlation of full wavefields. Our wavefield-separation imaging condition removes the image noise, and results in clean images of the layers and faults (Figs. 2b-d). The layers are best imaged using the downing source wavefields and upgoing receiver

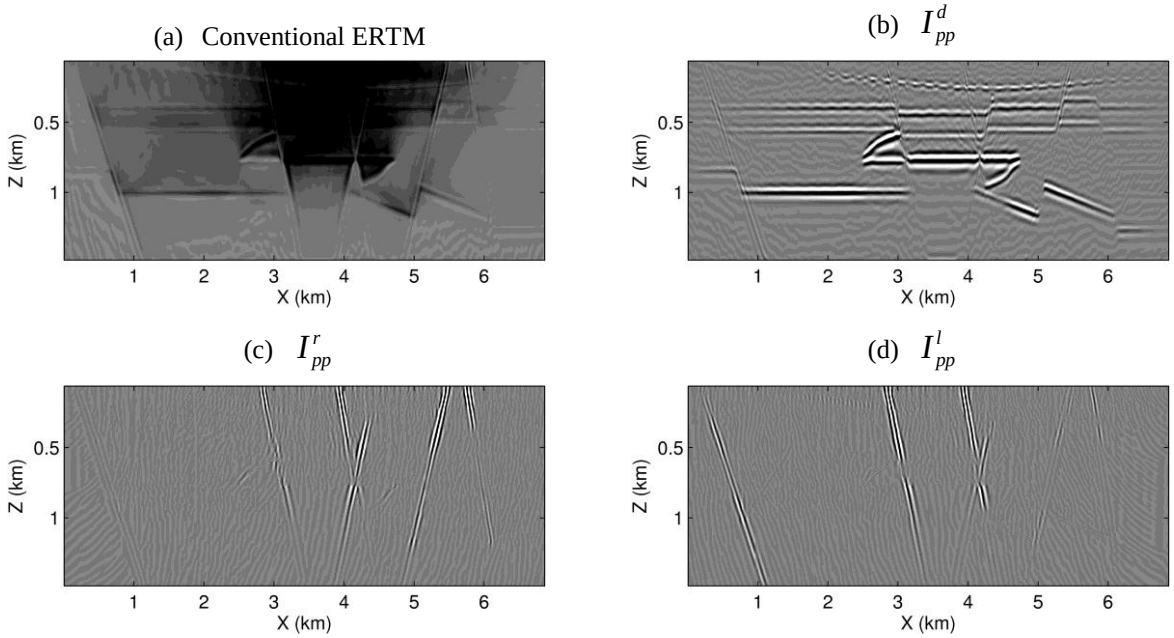

Figure 2: Comparison of PP images of the fault model for the Soda Lake geothermal field obtained with the conventional and new ERTM methods: (a) The conventional ERTM image, (b) downward-looking image, (c) right-looking image, and (d) left-looking image. Explosive sources are used.

wavefields (Fig. 2b). The image from the rightgoing source wavefields and leftgoing receiver wavefields illuminates mostly the faults on the right side of the model (Fig. 2c). The image obtained using the leftgoing source wavefields and rightgoing receiver wavefields illuminates mostly the faults on the left side of the model (Fig. 2d).

The PS images of the Soda Lake fault model using explosive sources are shown in Fig. 3. The image obtained using the conventional imaging condition shows destructive interfaces (Fig. 3a). The polarization problem is clearly observed along the horizontal reflectors. After wavefield separation, the images improve a little bit as shown in Figs. 3b, 3d, 3f, but the polarization problem still exists. The angle-domain analysis corrects for the polarization of converted waves, and shows coherent interfaces in Figs. 3c, 3e, 3g.

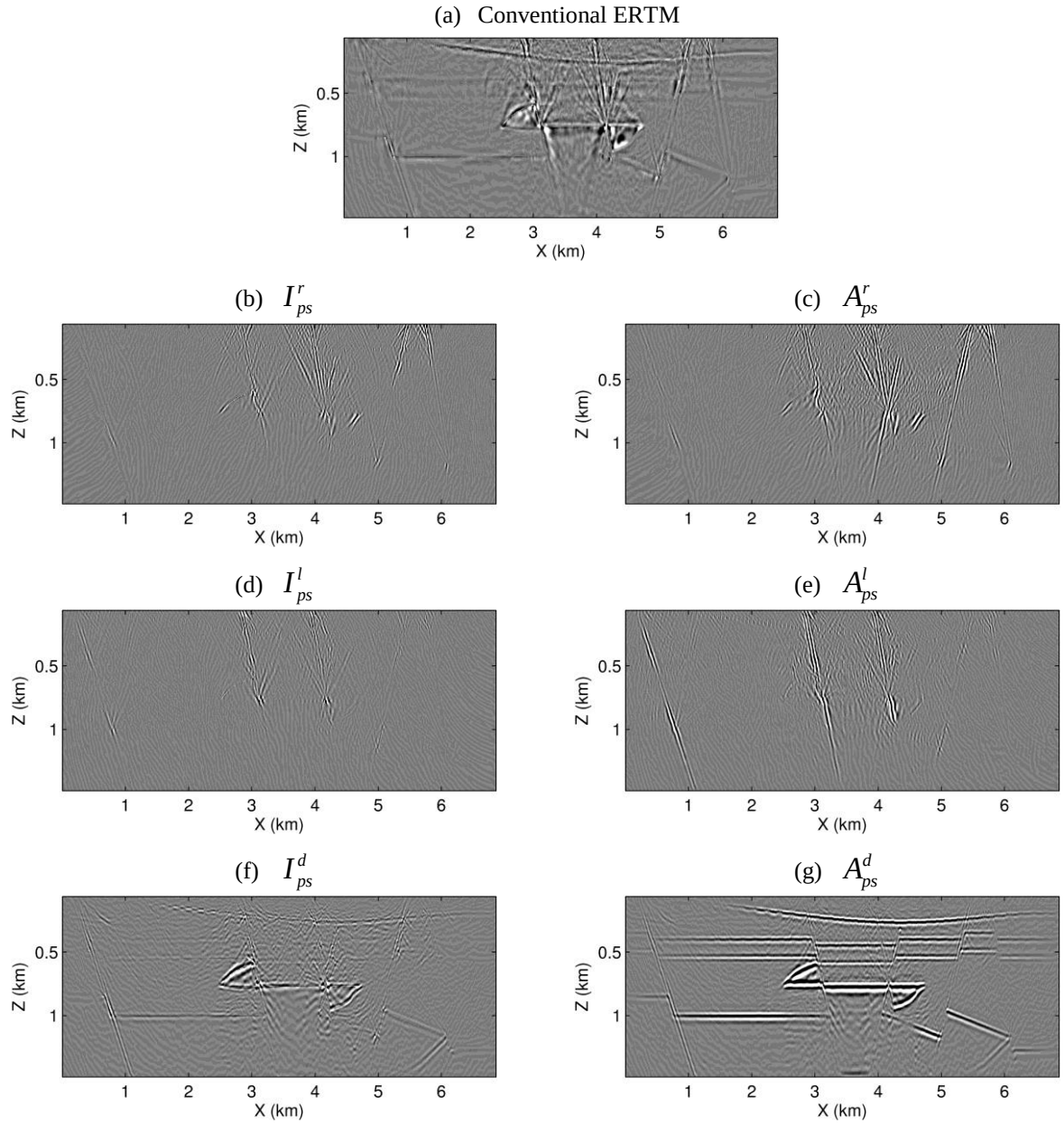

Figure 2: Comparison of PS images of the fault model for Soda Lake obtained with the conventional and new ERTM methods: (a) The conventional migration image, (b) right-looking image, (c) right-looking angle-domain image, (d) left-looking image, (e) left-looking angle-domain image, (f) downward-looking image, and (g) downward-looking angle-domain image. Explosive sources are used.

We obtain SP images of Soda Lake fault model using both horizontal- (Fig. 4) and vertical-force (Fig. 5) sources. The wavefield separation and angle-domain polarization correction result in more coherent images than the one obtained with the conventional imaging condition. The horizontal layers in the SP image produced using vertical-force sources (Fig. 5g) has more artifacts than that generated using horizontal-force sources (Fig. 4g) because of the weaker downgoing S-wave components in vertical-force sources. The SP image using horizontal- or vertical-force sources has more artifacts than PP and PS images using explosive sources because of the complication of two incident components (P and S) instead of one (P).

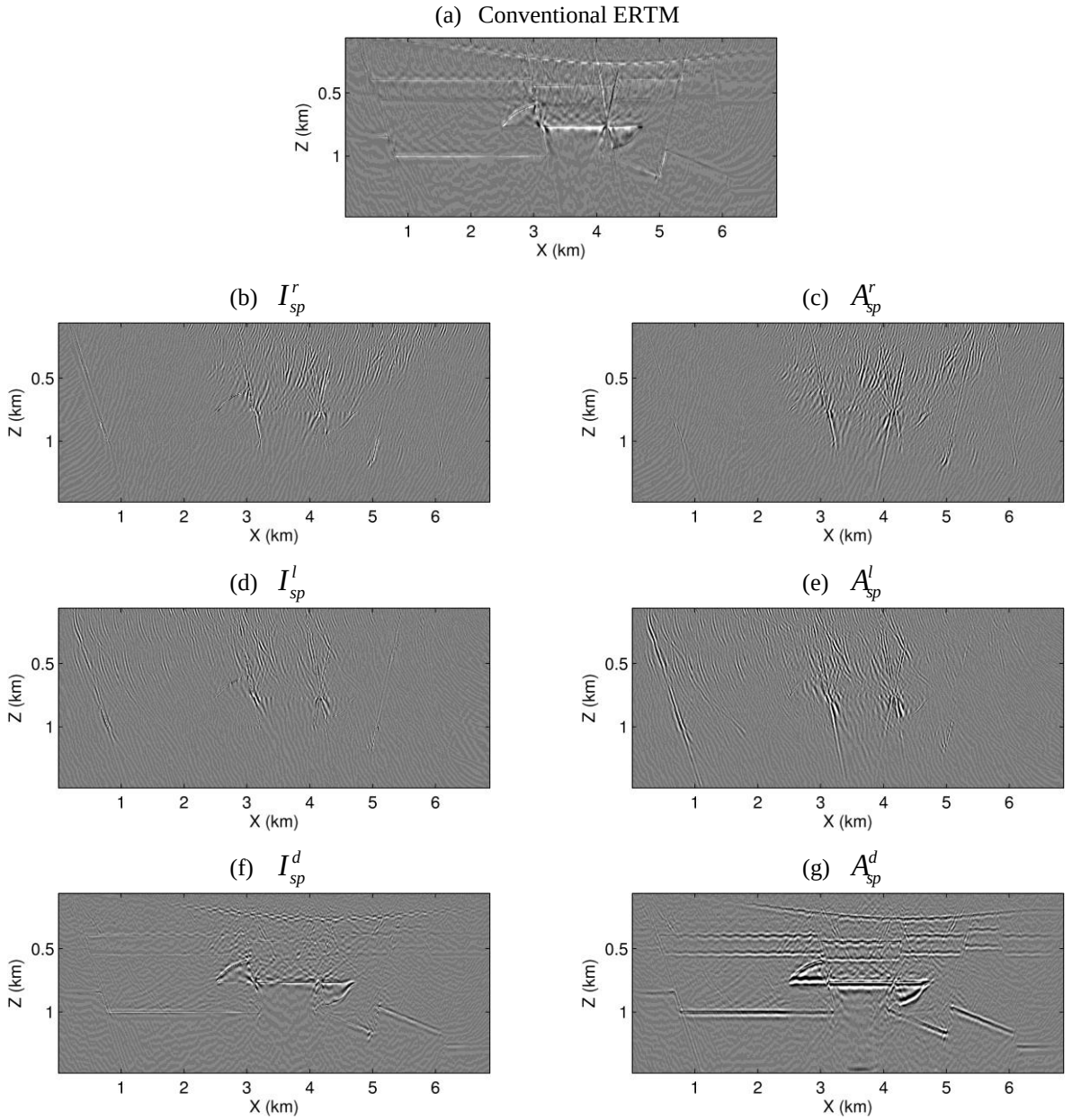

Figure 4: Comparison of SP images of the fault model for Soda Lake obtained with the conventional and new ERTM methods: (a) The conventional migration image, (b) right-looking image, (c) right-looking angle-domain image, (d) left-looking image, (e) left-looking angle-domain image, (f) downward-looking image, and (g) downward-looking angle-domain image. Horizontal-force sources are used.

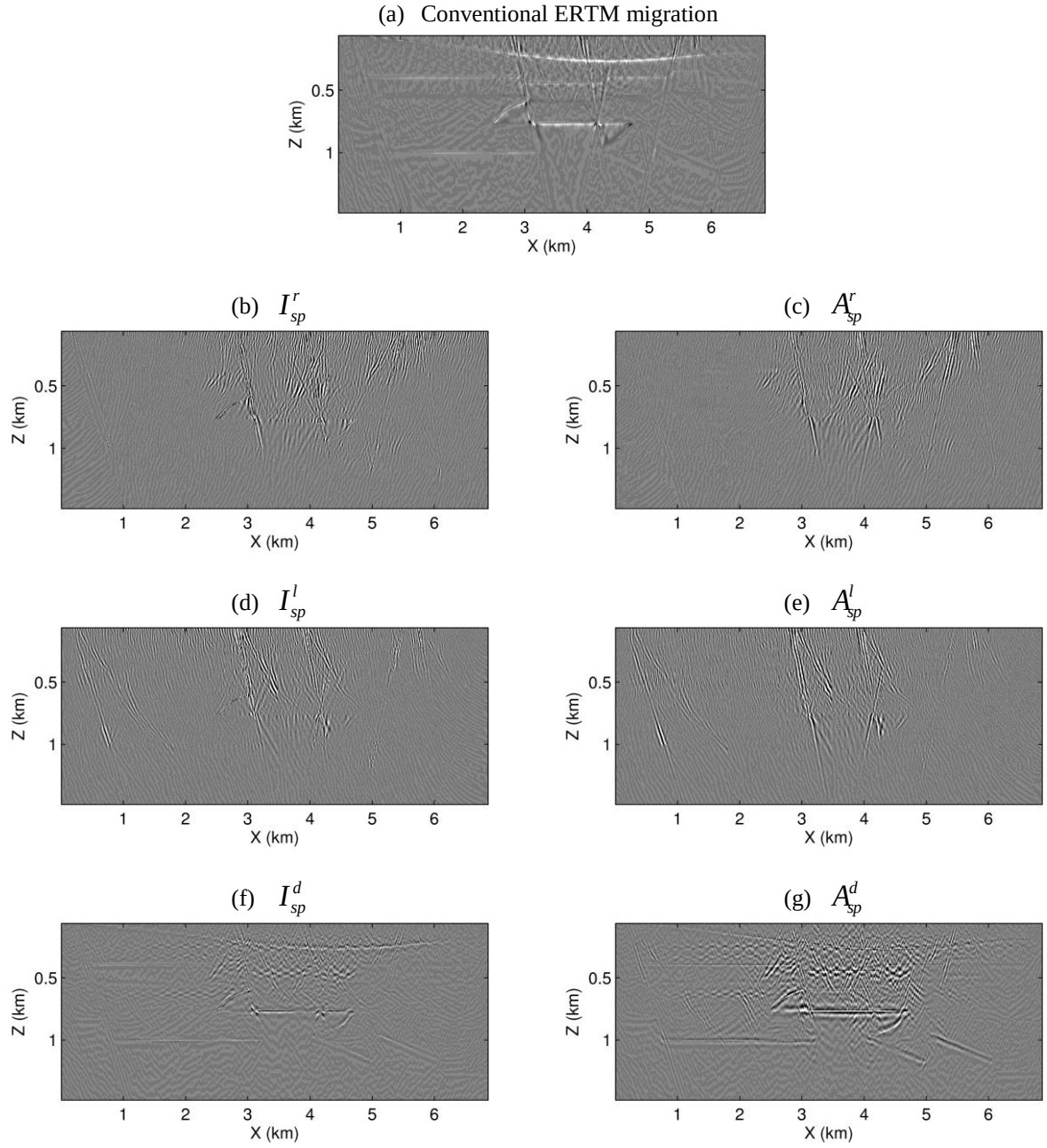

Figure 3: Comparison of SP images of the fault model for Soda Lake obtained with the conventional and new ERTM methods: (a) The conventional migration image, (b) right-looking image, (c) right-looking angle-domain image, (d) left-looking image, (e) left-looking angle-domain image, (f) downward-looking image, and (g) downward-looking angle-domain image. Vertical-force sources are used.

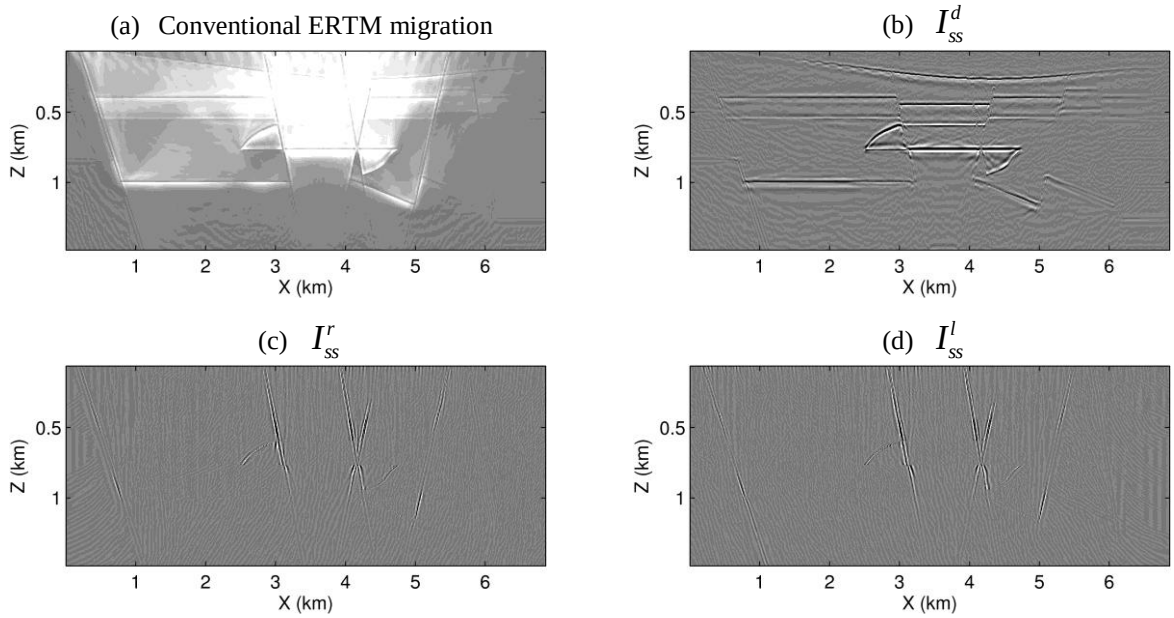

Figure 6: Comparison of SS images of the fault model for Soda Lake obtained with the conventional and new ERTM methods: (a) the conventional migration image, (b) downward-looking image, (c) right-looking image, and (d) left-looking image. Horizontal-force sources are used.

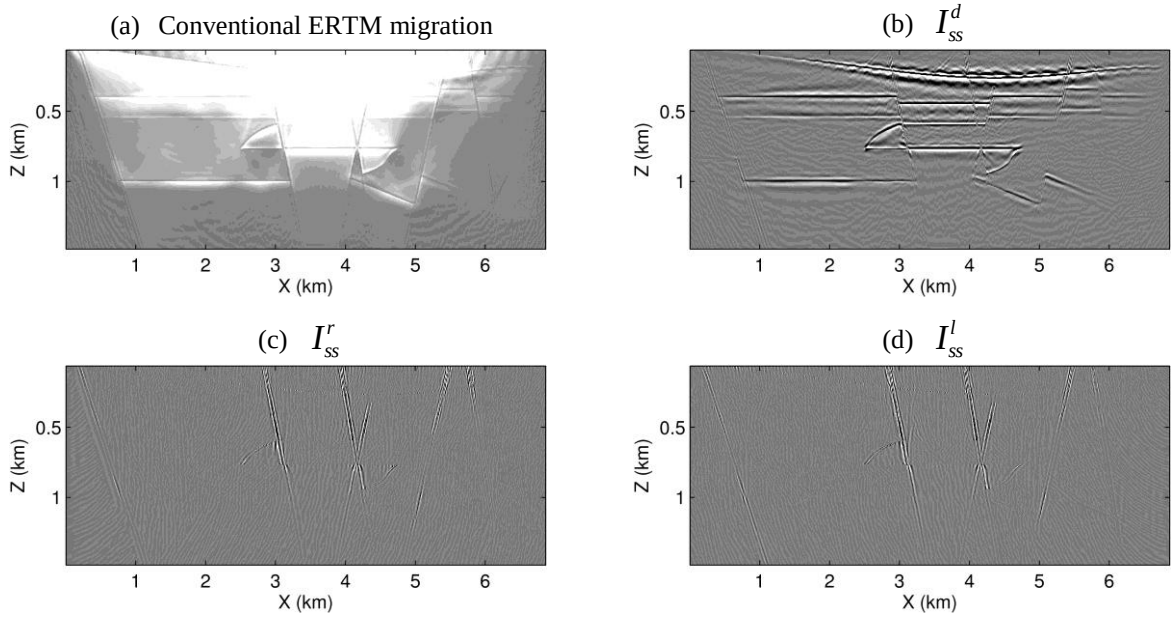

Figure 7: Comparison of SS images of the fault model for Soda Lake obtained with the conventional and new ERTM migration methods: (a) the conventional migration image, (b) downward-looking image, (c) right-looking image, and (d) left-looking image. Vertical-force sources are used.

We produce SS images of Soda Lake fault model using both horizontal- (Fig. 6) and vertical-force (Fig. 7) sources. The wavefield separation eliminates the high-amplitude and low-wavenumber background noise seen in the conventional ERTM image. The SS image produced using horizontal- and vertical-force sources are comparable, and seem to have the highest resolution compared with the PP, PS, and SP images because of the shorter wavelength of S waves than that of P waves.

CONCLUSIONS

We have developed a new elastic reverse-time migration method by combing wavefield separation and angle-domain image analysis. We use synthetic multi-component seismic reflection data for a 2D velocity model constructed using the geologic features found at the Soda Lake geothermal field to demonstrate that our new migration method can directly image steeply-dipping fault zones, and significantly improves over conventional elastic reverse-time migration. Specifically, it eliminates the high-amplitude and low-wavenumber background noise, and corrects the polarization problem for converted waves, thus produce clean images of PP, PS, SP, and SS. We have also found that multi-component seismic data from explosive sources yield best PP and PS images of fault zones, and seismic data acquired using vertical and horizontal sources give best SP and SS images of fault zones.

ACKNOWLEDGEMENTS

This work was supported by the Geothermal Technologies Program of the U.S. Department of Energy through contract DE-AC52-06NA25396 to Los Alamos National Laboratory. We thank James Echols for his help in building the velocity model for the Soda Lake geothermal field.

REFERENCES

Baysal, E., D. D. Kosloff, and J. W. C. Sherwood, (1983), "Reverse Time Migration," *Geophysics*, **48**, 1514–1524.

Chang, W.-F. and McMechan, G. (1987), "Elastic Reverse-Time Migration," *Geophysics*, **52**, 1365-1375.

Denli, H., and L. Huang, (2008), "Elastic-Wave Reverse-Time Migration with a Wavefield-Separation Imaging Condition," *78th Annual International Meeting, SEG, Expanded Abstracts*, 2346–2350.

Du, Q., Zhu, Y., and Ba, J. (2012), "Polarity Reversal Correction for Elastic Reverse Time Migration," *Geophysics*, **77**(2), S31-S41.

Huang, L. and M. Albrecht (2011), "Seismic and Magneto-Telluric Imaging for Geothermal Exploration at Jemez Pueblo in New Mexico," *Proceedings of the Thirty-Sixth Workshop on Geothermal Reservoir Engineering, Stanford University*, SGP-TR-191, 944-949.

Huang, L., Kelley, S., Zhang, Z., Rehfeldt, K., Albrecht, M., and Kaufman, G. (2011), "Imaging Faults with Reverse-Time Migration for Geothermal Exploration at Jemez Pueblo in New Mexico," *GRC Transactions*, **35**, 833-837.

Kaelin, B., and A. Guitton, (2006), "Imaging Condition for Reverse Time Migration," *76th Annual International Meeting, SEG, Expanded Abstracts*, 2594–2598.

Liu, F., Zhang, G., Morton, S. A., and Leveille, J. P. (2011), "An Effective Imaging Condition for Reverse-Time Migration Using Wavefield Decomposition," *Geophysics*, **76**(1), S29-S39.

McMechan, G. A., (1983), "Migration by Extrapolation Of Time-Dependent Boundary Values," *Geophysical Prospecting*, **31**, 413–420.

Mulder, W. A., and R.-E. Plessix, (2004), "A Comparison between One-Way and Two-Way Wave-Equation Migration," *Geophysics*, **69**, 1491–1504.

Whitmore, N. D., (1983), "Iterative Depth Migration by Backward Time Propagation," *53rd Annual International Meeting, SEG, Expanded Abstracts*, 382-385.

Yan, J., and Sava, P. (2008), "Isotropic Angle-Domain Elastic Reverse-Time Migration," *Geophysics*, **73**(6), S229-S239.

Yan, R., and X. B. Xie, (2010), "A New Angle-Domain Imaging Condition for Elastic Reverse-Time Migration," *80th Annual International Meeting, SEG, Expanded Abstracts*, 3181–3186.

Yoon, K., K. Marfurt, and E. W. Starr, (2004), "Challenges in Reverse-Time Migration," *74th Annual International Meeting, SEG, Expanded Abstract*, 1057-1060.